\



High efficiency ETM-free perovskite cell composed of CuSCN and increasing gradient $CH_3NH_3PbI_3$

Tao Wang(汪涛), Gui-Jiang Xiao(肖贵将), Ren Sun(孙韧), Lin-Bao Luo(罗林保), and Mao-Xiang Yi(易茂祥)
Citation: Chin. Phys. B, 2022, 31 (**1**): 018801. DOI: 10.1088/1674-1056/ac0bb0
Journal homepage: http://cpb.iphy.ac.cn; http://iopscience.iop.org/cpb

What follows is a list of articles you may be interested in

Non-peripherally octaalkyl-substituted nickel phthalocyanines used as non-dopant hole transport materials in perovskite solar cells

Fei Qi(齐飞), Bo Wu(吴波), Junyuan Xu(徐俊源), Qian Chen(陈潜), Haiquan Shan(单海权), Jiaju Xu(许家驹), and Zong-Xiang Xu(许宗祥)
Chin. Phys. B, 2021, 30 (**10**): 108801. DOI: 10.1088/1674-1056/ac1573

Stabilization of formamidinium lead iodide perovskite precursor solution for blade-coating efficient carbon electrode perovskite solar cells

Yu Zhan(占宇), Weijie Chen(陈炜杰), Fu Yang(杨甫), and Yaowen Li(李耀文)
Chin. Phys. B, 2021, 30 (**8**): 088803. DOI: 10.1088/1674-1056/abfbcb

Improved efficiency and stability of perovskite solar cells with molecular ameliorating of ZnO nanorod/perovskite interface and Mg-doping ZnO

Zhenyun Zhang(张振雲), Lei Xu(许磊), and Junjie Qi(齐俊杰)
Chin. Phys. B, 2021, 30 (**3**): 038801. DOI: 10.1088/1674-1056/abd748

Highly efficient bifacial semitransparent perovskite solar cells based on molecular doping of CuSCN hole transport layer

Shixin Hou(侯世欣), Biao Shi(石标), Pengyang Wang(王鹏阳), Yucheng Li(李玉成), Jie Zhang(张杰), Peirun Chen(陈沛润), Bingbing Chen(陈兵兵), Fuhua Hou(侯福华), Qian Huang(黄茜), Yi Ding(丁毅), Yuelong Li(李跃龙), Dekun Zhang(张德坤), Shengzhi Xu(许盛之), Ying Zhao(赵颖), Xiaodan Zhang(张晓丹)
Chin. Phys. B, 2020, 29 (**7**): 078801. DOI: 10.1088/1674-1056/ab99ae

Current improvement in substrate structured Sb_2S_3 solar cells with $MoSe_2$ interlayer

Lu Liu(刘璐), Sheng-Li Zhang(张生利), Jian-Yu Wu(吴建宇), Wei-Huang Wang(王伟煌), Wei Liu(刘玮), Li Wu(武莉), Yi Zhang(张毅)
Chin. Phys. B, 2020, 29 (**5**): 058801. DOI: 10.1088/1674-1056/ab8220

High efficiency ETM-free perovskite cell composed of CuSCN and increasing gradient $CH_3NH_3PbI_3$

Tao Wang(汪涛)[1,3,4,†], Gui-Jiang Xiao(肖贵将)[1], Ren Sun(孙韧)[2], Lin-Bao Luo(罗林保)[1], and Mao-Xiang Yi(易茂祥)[1]

[1] *School of Microelectronics, Hefei University of Technology, Hefei* 230601, *China*
[2] *School of Electronic Science and Engineering, Southeast University, Nanjing* 210096, *China*
[3] *School of Information Science and Technology, University of Science and Technology of China, Hefei* 230027, *China*
[4] *National Engineering Laboratory of Special Display Technology, Hefei* 230009, *China*

(Received 22 March 2021; revised manuscript received 10 May 2021; accepted manuscript online 16 June 2021)

To enhance device performance and reduce fabrication cost, a series of electron transporting material (ETM)-free perovskite solar cells (PSCs) is developed by TCAD Atlas. The accuracy of the physical mode of PSCs is verified, due to the simulations of PEDOT:PSS–$CH_3NH_3PbI_3$–PCBM and CuSCN–$CH_3NH_3PbI_3$–PCBM p–i–n PSCs showing a good agreement with experimental results. Different hole transporting materials (HTMs) are selected and directly combined with n-$CH_3NH_3PbI_3$, and the CuSCN–$CH_3NH_3PbI_3$ is the best in these ETM-free PSCs. To further study the CuSCN–$CH_3NH_3PbI_3$ PSC, the influences of back electrode material, gradient band gap, thickness, doping concentration, and bulk defect density on the performance are investigated. Energy band and distribution of electric field are utilized to optimize the design. As a result, the efficiency of CuSCN–$CH_3NH_3PbI_3$ PSC is achieved to be 26.64%. This study provides the guideline for designing and improving the performances of ETM-free PSCs.

Keywords: electron transporting material (ETM)-free perovskite solar cell, inorganic hole transporting material (HTM), back electrode, gradient band gap

PACS: 88.40.hj, 88.40.fc, 88.40.H– **DOI:** 10.1088/1674-1056/ac0bb0

1. Introduction

With high absorption coefficient, long carrier lifetime, high mobility and other good photoelectric characteristics, $CH_3NH_3PbI_3$ has been the subject of extensive research interest recently, and the efficiency of organic–inorganic hybrid perovskite solar cell (PSC) has reached 24.2%.[1] Obviously, the power conversion efficiency (PCE) of PSC is determined by the materials and structures of PSC.[2,3] To explore high-performance PSC, it is of great significance to construct p–i–n or p–n structures by the combination of perovskite and some organic or inorganic materials.

Some performances of p–i–n structure are better than those of n–i–p structure under the same material according to relevant researches, such as *J*–*V* curve hysteresis and fill factor.[2–5] A typical inverted planar PSC with p–i–n structure is usually composed of five layers, *i.e.*, electron transporting material (ETM), hole transporting material (HTM), perovskite absorption material, transparent conducting oxides (TCO), and back electrode. Fullerene (C_{60}, C_{70}) and phenyl-C_{61}-butyric acid methyl ester (PCBM) are the most commonly ETM in p–i–n PSC.[3–6] However, the PCE of the PSC is strictly limited by fullerene and PCBM due to their poor conductivities, multiple pinholes and rough topographies. Moreover, fullerene and PCBM are unstable in ambient condition and expensive due to the complex fabrication process.[6,7] Undoubtedly, these factors seriously hinder the applications of p–i–n PSC with fullerene or PCBM acting as ETM.

Compared with p–i–n PSCs, ETM-free PSC possesses many benefits, such as reduced cost, simplified technology and improved stability. In recent years, the ETM-free PSC has received much attention.[8–13] Inverted ETM-free PSC was fabricated first by Deng *et al.* with ITO-PEDOT:PSS–$CH_3NH_3PbI_3$–Au structure, but the efficiency was only 4.06%.[8] In 2018, PCE of ETM-free PSC was achieved to be 18.1% due to the increased matching of different band gaps materials in ITO–PTAA–$MAPbI_3$–Ti structure.[9] Subsequently, simulation efficiency of ETM-free PSC achieved 22.25% by optimizing the thickness and band offset of materials.[10] Although some ETM-free PSCs have been manufactured, the lack of research on the internal mechanism of PSC hinders the fabrication and application of cell. Furthermore, there are some shortcomings of PEDOT:PSS and PTAA, for instance, they are poor in conductivity, expensive and easily decomposed.[11]

Recently, some inorganic materials with good stability and high mobility have been widely studied, such as CuSCN, CuO, Cu_2O, CuI, and NiO.[12,13] However, these materials have not been used to enhance performance of ETM-free PSC so far. Moreover, as a common electrode material for PSC, Au is expensive and there is a Schottky barrier at the Au–

†Corresponding author. E-mail: taowang@hfut.edu.cn

© 2022 Chinese Physical Society and IOP Publishing Ltd

$CH_3NH_3PbI_3$ interface. Moreover, the influences of two-dimensional electric field, gradient band gap, doping concentration, and bulk defects on the performance of ETM-free PSC have not been reported.

Here in this work, the n-type $CH_3NH_3PbI_3$, as an absorber, is combined with HTM to form a p–n heterojunction ETM-free PSC. This geometry can form an effective built-in electric field which will allow the photo-generated carriers to be separated under illumination, the carriers to transfer form heterojunction to HTM or n-type $CH_3NH_3PbI_3$, and the carriers to be collected by the front electrode and the back electrode. Based on TCAD Atlas software, the structural characteristics, material selection, band gap design and some parameters optimization of ETM-free PSC are studied in detail. Some crucial properties, *i.e.*, energy band of heterojunction, two-dimensional distribution of electric field, and recombination rate are characterized.

2. Model calibration and parameters of materials

Since the excitons are of typical Wannier-type in perovskite material, the transport of photogenerated carriers in organic and inorganic materials could be treated with the same method.[14] To ensure the accuracy of the physical model, TCAD simulation of typical plane heterojunction PSC published by Aaesha *et al.*[15] is repeated and calibrated. The device structure of Ref. [15] (FTO–TiO_2–$CH_3NH_3PbI_3$–Spiro-OMETAD-Silver) is illustrated in Fig. 1(a). The *J*–*V* characteristic simulated by our model is compared with that from Ref. [15] as shown in Fig. 1(b). Physical model is calibrated by the two consistent *J*–*V* curves. Based on inverted p–i–n PSCs (HTM-$CH_3NH_3PbI_3$-ETM), the p–n ETM-free PSCs (HTM-$CH_3NH_3PbI_3$) are studied and compared with p–i–n PSCs. Schematic structures of two types of PSCs are shown in Figs. 1(c)–1(d).

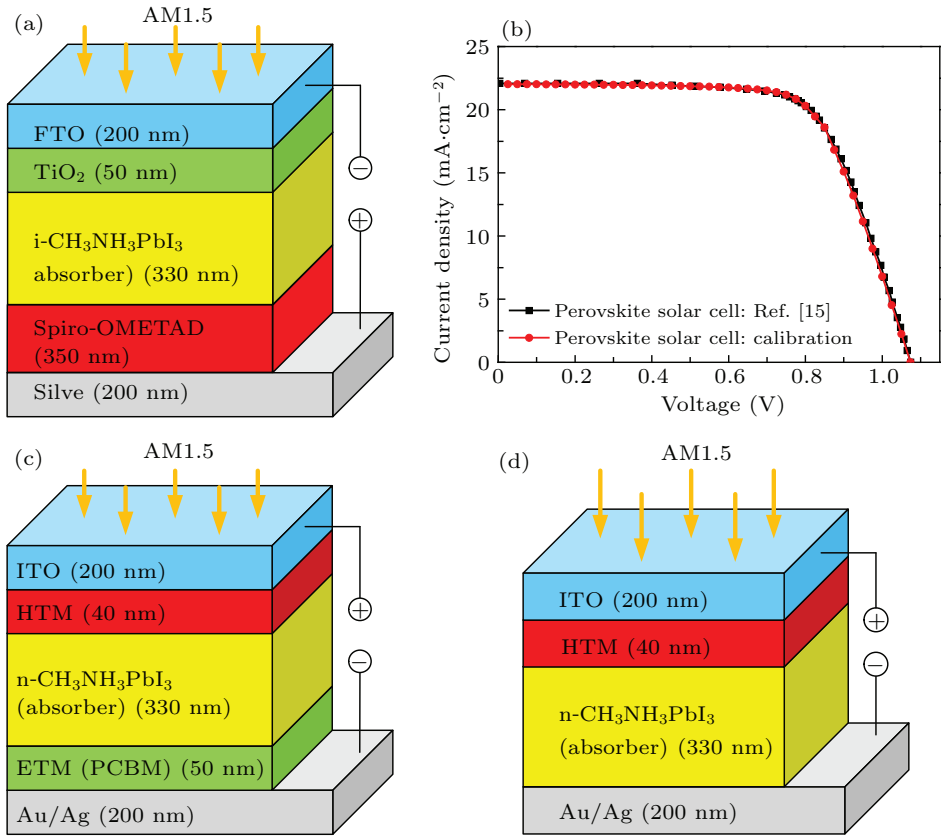


Fig. 1. (a) Device structure of PSC in Ref. [15], (b) *J*–*V* characteristics, (c) structure of p–i–n PSC, and (d) structure of ETM-free PSC.

The physics parameters of each type of materials that are obtained from the literature[12,14–21] are listed in Table 1, where ε_r is the relative permittivity, χ is the electron affinity, μ_n and μ_p represent mobility of electron and hole, respectively, τ_n is the electron lifetime, τ_p is the hole lifetime, E_g is the band gap, N_c and N_v represent the effective density of states in conduction band and valence band, respectively, N_a and N_d are acceptor and donor densities, respectively, τ_n and τ_p in PCBM are calculated by the Einstein relation and diffusion length of carriers.[15,20] Refractive index (n) and extinction coefficient (k) of materials are utilized from the literature.[22–27] The Newton iterative method is used to solve nonlinear equations during simulation. The contact between semiconductor and metal is considered as an ideal ohmic contact. The device non-contact boundary conditions are considered as the ideal Neumann boundary conditions. Fermi–Dirac statistical

distribution, indirect recombination, Shockley–Read–Hall recombination and Auger recombination models are considered in PSC. Moreover, the bulk defects of HTM, ETM, and perovskite are cited from the literature.[28–34] The influence of interface defect on the PSC is described by interface recombination rate (IRR), and the IRR of heterojunction interface is set to be 1000 cm/s. Light condition is AM 1.5 and 100 mW/cm^2. Temperature is 300 K.

Table 1. Simulation parameters of inverted p–i–n PSCs and ETM-free PSCs.[12–28]

Parameter	PEDOT:PSS	CuO	Cu_2O	CuSCN	NiO	CuI	$CH_3NH_3PbI_3$	PCBM
Thickness (nm)	40	40	40	40	40	40	330	50
ε_r	3.0	10.26	7.11	10	10.7	6.5	6.5	4.0
χ (eV)	2.2	4.1	3.2	1.7	1.46	2.1	3.9	3.9
E_g (eV)	3.0	1.3	2.17	3.6	3.8	3.1	1.55	2.0
N_c (cm^{-3})	2.2×10^{15}	2.32×10^{19}	2.0×10^{17}	2.2×10^{19}	2.8×10^{19}	2.8×10^{19}	4.42×10^{17}	1.0×10^{21}
N_v (cm^{-3})	1.8×10^{18}	5.57×10^{20}	1.1×10^{19}	1.8×10^{18}	1.0×10^{19}	1.0×10^{19}	8.47×10^{18}	2.0×10^{20}
μ_n (cm^2·V^{-1}·s^{-1})	1.0	34.5	200	100	12	100	1.62	0.01
μ_p (cm^2·V^{-1}·s^{-1})	40	2.0	80	25	2.8	43.9	1.62	0.01
N_a (cm^{-3})	1.0×10^{19}	1.0×10^{18}	1.0×10^{18}	1.0×10^{18}	1.0×10^{18}	1.0×10^{18}	0	0
N_d (cm^{-3})	0	0	0	0	0	0	1.0×10^{16}	1.0×10^{17}
τ_n (s)	5.29×10^{-5}	4.6×10^{-10}	1.0×10^{-8}	1.8×10^{-4}	6.42×10^{-9}	2.0×10^{-10}	2.88×10^{-7}	1.2×10^{-6}
τ_p (s)	5.29×10^{-5}	4.6×10^{-10}	1.0×10^{-7}	1.8×10^{-4}	6.42×10^{-9}	2.0×10^{-10}	2.88×10^{-7}	1.2×10^{-6}

3. Results and discussion

3.1. Simulated performance of ETM-free PSCs and inverted p–i–n PSCs

To investigate the difference between inverted p–i–n PSCs and ETM-free PSCs, four types of PSCs with different structures are studied, *i.e.*, PEDOT:PSS–$CH_3NH_3PbI_3$–PCBM, CuSCN–$CH_3NH_3PbI_3$–PCBM, PEDOT:PSS–$CH_3NH_3PbI_3$, and CuSCN–$CH_3NH_3PbI_3$. I–$CH_3NH_3PbI_3$ with a doping concentration of 1.0×10^{13} cm^{-3} acting as an absorber and PCBM serving as ETM in these p–i–n PSCs. Based on the inverted p–i–n PSC, the ETM-free PSC is designed when PCBM layer is removed and n-$CH_3NH_3PbI_3$ is self-doped by donors with a concentration of 1.0×10^{16} cm^{-3}.

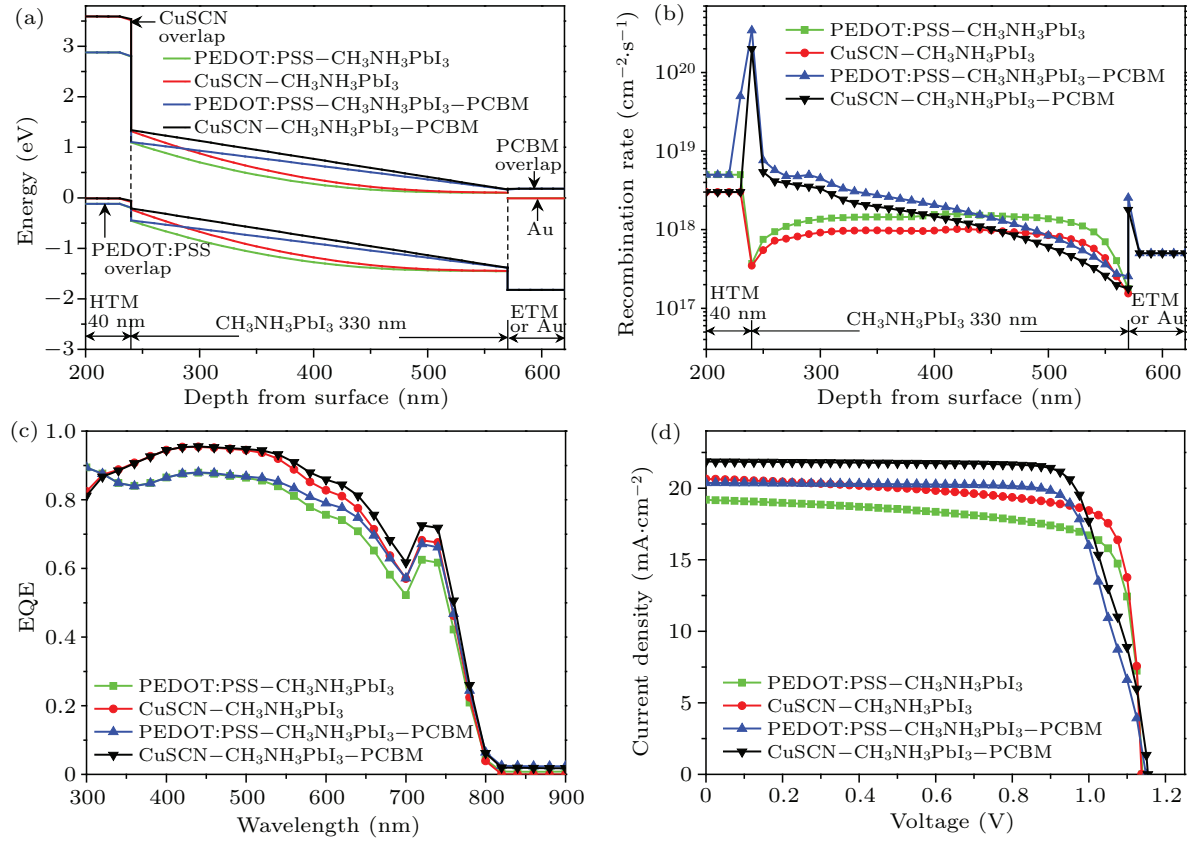


Fig. 2. Comparison of performance between ETM-free PSCs and p–i–n PSCs: (a) energy band, (b) recombination rate, (c) EQE, and (d) *J*–*V* characteristics.

The energy bands of the four PSCs are illustrated in Fig. 2(a). When p–i–n PSCs are simplified into ETM-free PSCs, bending trend of energy band of $CH_3NH_3PbI_3$ is converted from "linear gradient" type into "abruptly curved" type, which is beneficial for impeding both photogenerated electrons from diffusing into anode and photogenerated holes from diffusing into cathode, leading the reverse saturation current to decrease. Simultaneously, the bending quantities of the energy band of $CH_3NH_3PbI_3$ for p–i–n PSCs and ETM-free PSCs are equal, which means that the total built-in potential difference (V_D) is equal. However, comparing with p–i–n PSCs, the V_D at 240 nm–450 nm depth of $CH_3NH_3PbI_3$ in ETM-free PSCs is big. As a result, recombination rate in $CH_3NH_3PbI_3$ of ETM-free PSCs is obviously smaller than that of p–i–n PSCs as shown in Fig. 2(b), so that more electron–hole pairs will be separated and collected in ETM-free PSCs.

The external quantum efficiency (EQE) of PSCs is illustrated in Fig. 2(c). Comparing with p–i–n PSC, the EQE of ETM-free PSC slightly decreases in a wavelength range of 450 nm–750 nm. Simultaneously, the EQE of CuSCN is higher than that of PEDOT:PSS in a wavelength range of 330 nm–750 nm, because the electron mobility of inorganic CuSCN (100 $cm^2 \cdot V^{-1} \cdot s^{-1}$) is much higher than that of organic PEDOT:PSS (1 $cm^2 \cdot V^{-1} \cdot s^{-1}$). The *J*–*V* characteristics of four PSCs are shown in Fig. 2(d). If the graph enveloped by *J*–*V* curve and coordinate axis is more matched to rectangle, the fill factor (*FF*) of the PSC is higher.[5] Obviously, the *FF* of ETM-free PSC is better than that of p–i–n PSC due to the fact that the graph enveloped by coordinate axis and the *J*–*V* curve of the former is closer to a rectangle than that of the latter. In ETM-free PSC, the n-$CH_3NH_3PbI_3$ is heavily doped, the conductivity of material is improved and series resistance (R_s) is reduced, resulting in the compensated *FF*.

Simulated performances of four PSCs are listed in Table 2. Obviously, the simulation results are closely coincided with experimental results of p–i–n PSCs, which confirms the reliability of the physical model. Meanwhile, the efficiency of CuSCN–$CH_3NH_3PbI_3$ PSC is 18.56%, which is higher than that of PEDOT:PSS–$CH_3NH_3PbI_3$–PCBM PSC (18.06%), but lower than that of CuSCN–$CH_3NH_3PbI_3$–PCBM (19.56%). Obviously, the efficiency of ETM-free PSC decreases down to less than 1.29% by simplifying p–i–n structure, which means that the high efficiency can be achieved by ETM-free PSC with simplified preparation process.

The detailed electric field distribution is shown in Fig. 3. Comparing with p–i–n PSC, the electric field intensity in ETM-free PSC is strong in a depth range of 240 nm–450 nm but weak in a depth range of 450 nm–570 nm. Since the generation rate of carriers in absorber decreases exponentially with the increase of thickness, the electron–hole pairs are concentrated mainly on the front surface of $CH_3NH_3PbI_3$. As a result, the velocity of the carriers in ETM-free PSCs is faster than that in the p–i–n PSCs, thus the electron–hole pairs will be separated faster and the recombination losses of the carriers will be less.

Photogenerated carriers will increase if thickness of $CH_3NH_3PbI_3$ increases, but the effects on ETM-free PSCs and p–i–n PSCs are quite different. It is obvious that the values of J_{sc} of four PSCs increase with a similar tendency while V_{oc}, *FF*, and PCE change are quite different when thickness of $CH_3NH_3PbI_3$ increases as illustrated in Figs. 4(a)–4(d).

When the thickness of i-$CH_3NH_3PbI_3$ in p–i–n PSC increases, the electric field in $CH_3NH_3PbI_3$ layer remains uniform and gradually decreases, but the distance of carriers transport to electrode increases, leading the bulk recombination losses to increase and V_{oc} to decrease. Meanwhile, the series resistance of p–i–n PSC increases rapidly due to low conductivity of i-$CH_3NH_3PbI_3$ and *FF* decreasing. The PCE of p–i–n PSCs increases at first because the J_{sc} increases, and then the PCE decrease subtly because V_{oc} and *FF* decrease.

In ETM-free PSCs, heavily doped n-$CH_3NH_3PbI_3$ gives rise to good conductivity and electronic transport capability. Meanwhile, the electric field in n-$CH_3NH_3PbI_3$ keeps unchanged as the thickness of $CH_3NH_3PbI_3$ increases, so recombination losses caused by multiple defects are almost unchanged but photogenerated carriers are increased obviously, so V_{oc}, J_{sc}, the *FF* and PCE of ETM-free PSCs keep increasing. Moreover, the PCE of ETM-free PSCs will exceed that of p–i–n type PSC when the thickness of $CH_3NH_3PbI_3$ is over 800 nm, which indicates that the ETM-free PSC can achieve higher PCE when the $CH_3NH_3PbI_3$ layer is thicker.

Table 2. Comparison of performance between ETM-free PSCs and p–i–n PSCs.

Type	Structure	HTM	Experiment	V_{oc} (V)	J_{sc} ($mA \cdot cm^2$)	*FF* (%)	PCE (%)
p–i–n	PEDOT:PSS–$CH_3NH_3PbI_3$–PCBM	organic	experiment[2]	1.1	20.9	79.00	18.1
			this work	1.15	20.58	76.31	18.06
	CuSCN–$CH_3NH_3PbI_3$–PCBM	inorganic	experiment[29]	1.1	20.76	73.00	16.66
			this work	1.15	21.86	77.56	19.56
p–n (ETM-free)	PEDOT:PSS–$CH_3NH_3PbI_3$	organic	this work	1.14	19.18	76.73	16.77
	CuSCN–$CH_3NH_3PbI_3$	inorganic	this work	1.14	20.64	79.07	18.56

According to Figs. 4(a)–4(d), CuSCN–$CH_3NH_3PbI_3$ PSC shows good performance in comparison with other configurations. The PCE of CuSCN–$CH_3NH_3PbI_3$ PSC is almost saturated when $CH_3NH_3PbI_3$ thickness is larger than 1000 nm. Therefore, 1000 nm is the most suitable thickness for $CH_3NH_3PbI_3$. Comparing with the famous organic PEDOT:PSS, the performance of CuSCN–$CH_3NH_3PbI_3$ is obviously better than that of PEDOT:PSS–$CH_3NH_3PbI_3$, which means that efficiency can be improved if $CH_3NH_3PbI_3$ directly contacts the inorganic HTM.

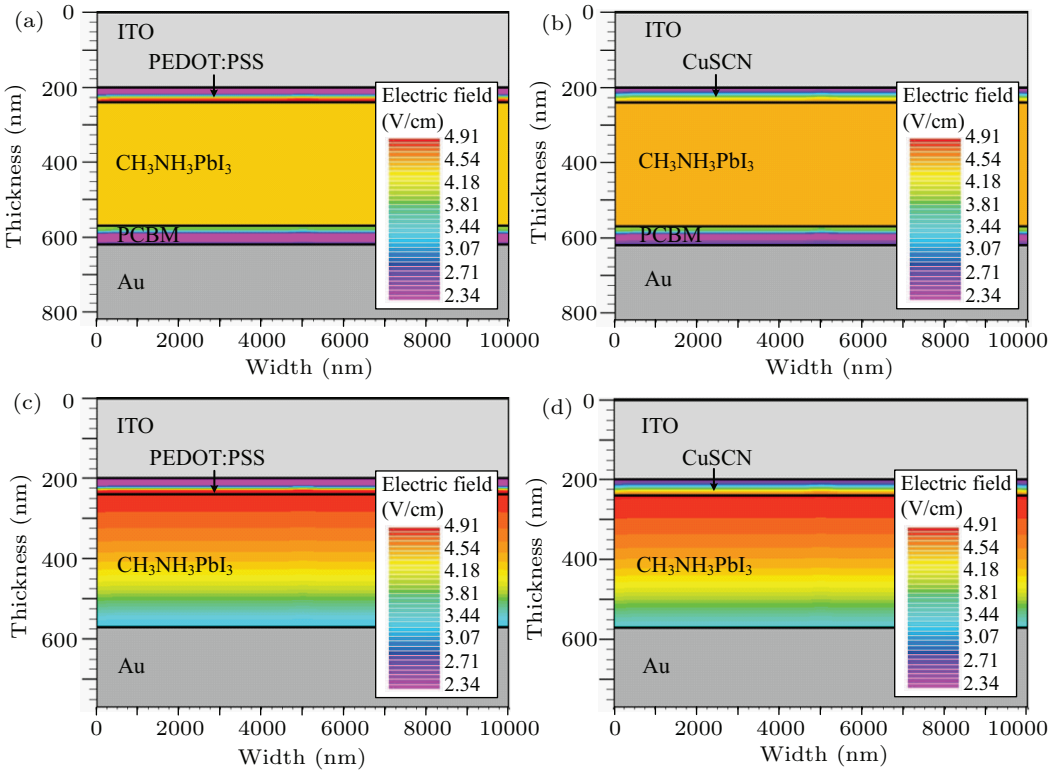


Fig. 3. Electric field distributions of different structures: (a) PEDOT:PSS–$CH_3NH_3PbI_3$–PCBM; (b) CuSCN–$CH_3NH_3PbI_3$–PCBM; (c) PEDOT:PSS–$CH_3NH_3PbI_3$; (d) CuSCN–$CH_3NH_3PbI_3$.

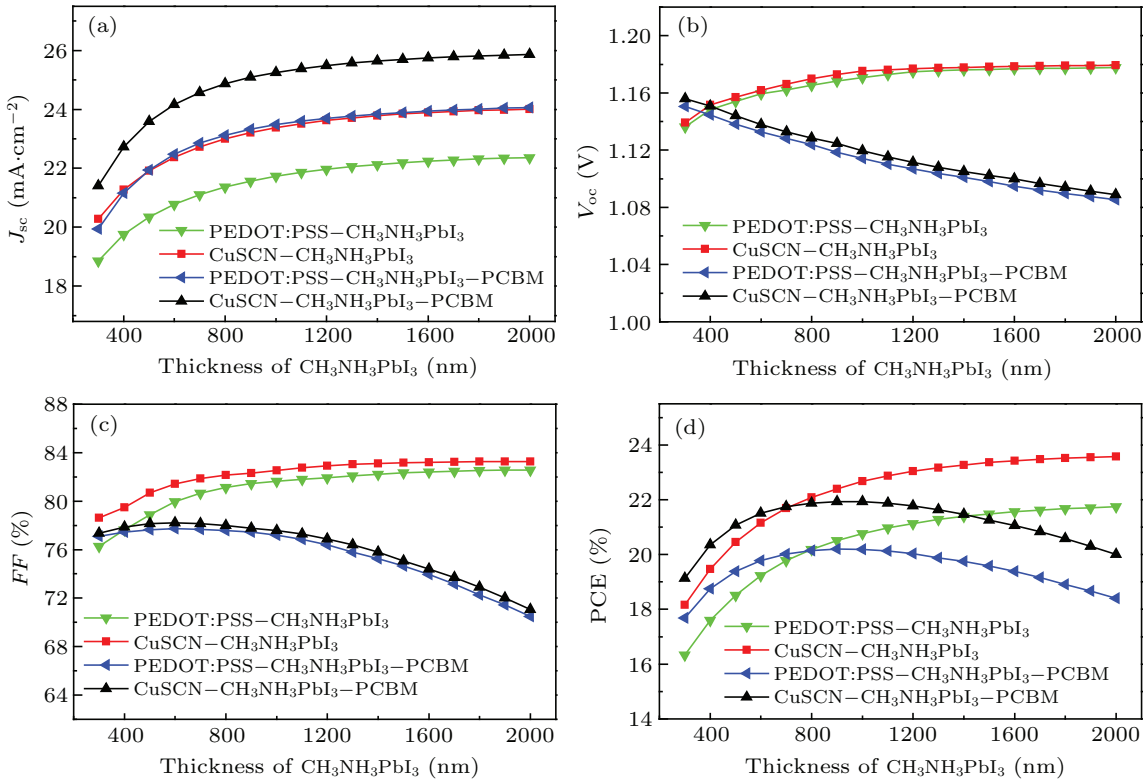


Fig. 4. Influences of $CH_3NH_3PbI_3$ thickness on performances of ETM-free PSC and p–i–n PSC: thickness-dependent: (a) J_{sc}, (b) V_{oc}, (c) FF, and (d) PCE.

3.2. Comparative study of CuSCN–$CH_3NH_3PbI_3$ and some typical ETM-free PSCs

In order to study the ETM-free PSCs in depth, five types of ETM-free PSCs are designed by a 330-nm-thick n-$CH_3NH_3PbI_3$ directly combined with different inorganic HTMs, *i.e.*, CuO, Cu_2O, CuI, NiO, and CuSCN. To study the influence of band structure on PSC performance, CuO and Cu_2O are selected to compare with the wide band gap materials, such as CuSCN, NiO, and CuI. The energy bands of five ETM-free PSCs are illustrated in Fig. 5(a). That the energy band barrier of $CH_3NH_3PbI_3$ in a space charge region is steeper means higher potential difference and stronger built-in electric field.[20] That the electronic barrier at HTM-$CH_3NH_3PbI_3$ interface is higher means smaller reverse saturation current from absorption layer to anode.[19] The values of ΔE_c of NiO–$CH_3NH_3PbI_3$ and CuSCN–$CH_3NH_3PbI_3$ interfaces are the largest, thus reverse saturation currents of the two PSCs are the smallest.

The *J*–*V* characteristics of PSCs are shown in Fig. 5(b). Obviously, V_{oc} and J_{sc} of CuO–$CH_3NH_3PbI_3$ is the smallest among the five PSCs. Because the band gap of CuO is 1.3 eV and the lowest electronic barrier is constructed on CuO–$CH_3NH_3PbI_3$ interface, which causes serious parasitic absorption (Fig. 5(c)) and large reverse saturation current. The CuI, NiO, and CuSCN show significant improvement in *J*–*V* curve, for these materials exhibit higher E_g and higher barrier at HTM–$CH_3NH_3PbI_3$ interface. Moreover, the best *FF* is obtained by CuSCN–$CH_3NH_3PbI_3$. The *FF* is determined by the energy level matching and series/parallel resistance.[30] An energy barrier of 0.15 eV between the highest occupied molecular orbitals (HOMOs) of CuSCN and perovskite is smaller than that of CuI and NiO, thus parasitic resistance is smaller.

Table 3 provides the simulation results of ETM-free PSCs. The PCE of CuI–$CH_3NH_3PbI_3$, NiO–$CH_3NH_3PbI_3$, CuSCN–$CH_3NH_3PbI_3$, Cu_2O–$CH_3NH_3PbI_3$, and CuO–$CH_3NH_3PbI_3$ PSC is 17.70%, 18.04%, 18.56%, 16.48%, and 13.88%, respectively. Comparatively, CuSCN–$CH_3NH_3PbI_3$ possesses the best structure and its PCE is achieved to be 18.56%. The EQEs of five ETM-free PSCs are shown in Fig. 5(c). The EQE of CuSCN–$CH_3NH_3PbI_3$ is the highest in a wavelength range of 350–450 nm.

Figure 5(d) shows the absorbance (A), reflectance (R), and transmittance (T) of CuSCN–$CH_3NH_3PBI_3$ PSC in detail. Reflection loss caused by material refractive index mismatch is 3.61 mA/cm^2; transmission loss caused by insufficient absorption is 5.47 mA/cm^2. Moreover, the absorption loss caused by the parasitic absorption of CuSCN is 0.26 mA/cm^2.

As shown in Tables 2 and 3 and Fig. 5, comparing with organic PEDOT:PSS and other four typical inorganic HTMs, *i.e.* CuO, Cu_2O, CuI, and NiO, the high performance ETM-free PSC can be achieved if HTM is selected as CuSCN.

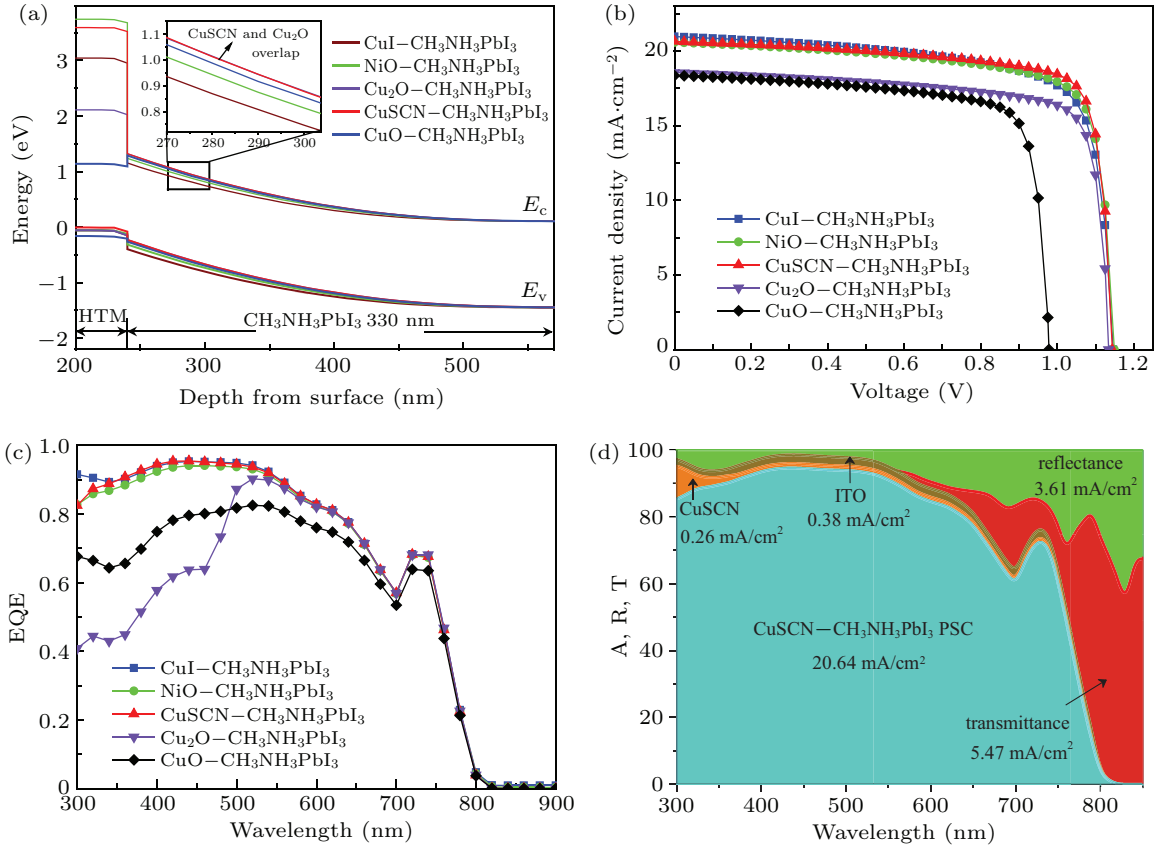


Fig. 5. Comparison of performance among ETM-free PSCs, showing (a) energy band *versus* depth, (b) *J*–*V* characteristics, (c) EQE *versus* wavelength, (d) absorbance (A), reflectance (R), and transmittance (T) *versus* wavelength of CuSCN–$CH_3NH_3PbI_3$ PSC.

Table 3. Simulated performances of five ETM-free PSCs with different inorganic HTMs.

Structure	V_{oc} (V)	J_{sc} (mA/cm^2)	*FF* (%)	PCE (%)
CuI–$CH_3NH_3PbI_3$	1.15	20.98	73.65	17.70
NiO–$CH_3NH_3PbI_3$	1.15	20.58	76.34	18.04
CuSCN–$CH_3NH_3PbI_3$	1.14	20.64	79.07	18.56
Cu_2O–$CH_3NH_3PbI_3$	1.13	18.57	78.29	16.48
CuO–$CH_3NH_3PbI_3$	0.98	18.36	77.33	13.88

3.3. Work function of back electrode on performance of CuSCN–$CH_3NH_3PbI_3$ PSC

The work function of back electrode plays an important role on built-in electric field of PSC and recombination rate of carrier. Work functions of some typical electrode materials, *i.e.* FTO, Ag, Ti, AZO, ITO, and Au are −4.0 eV, −4.26 eV, −4.33 eV, −4.4 eV, −4.8 eV, and −5.1 eV, respectively. To select an optimal back electrode, the influence of the back electrode work function on CuSCN–$CH_3NH_3PbI_3$ PSC performance is studied. The energy bands of the CuSCN–$CH_3NH_3PbI_3$ are shown in Fig. 6 with different back electrodes. The energy band of $CH_3NH_3PbI_3$ gradually sinks down and the Schottky barrier between $CH_3NH_3PbI_3$ and the back electrode decreases gradually with the increase of the back electrode work function, which reduces the electron backflow to the electrode and the accumulation of photogenerated electrons in the barrier region. Therefore, the recombination rate of electron-hole pairs decreases. When the material of the back electrode is FTO, the height of the Schottky barrier on the back surface of $CH_3NH_3PbI_3$ is equal to 0. At the moment, $CH_3NH_3PbI_3$ and FTO form a good energy band match. Therefore, in order to achieve a good charge transfer, the FTO is a suitable back electrode material.

Figure 7(a) shows the influence of the back electrode work function on the performance of CuSCN–$CH_3NH_3PBI_3$ PSC. The PCE increases linearly with the back electrode work function increasing from −5.2 eV to −4.0 eV. Once the work function exceeds −4.0 eV, the PCE of the PSC tends to be saturated. Therefore, in order to achieve a good PCE value, the back electrode work function of CuSCN–$CH_3NH_3PBI_3$ PSC should not be less than −4.0 eV. In addition, when the work function of back electrode is −4.0 eV, the *J*–*V* characteristic curve of CuSCN–$CH_3NH_3PbI_3$ PSC is overlapped with Ohmic contact curve as shown in Fig. 7(b).

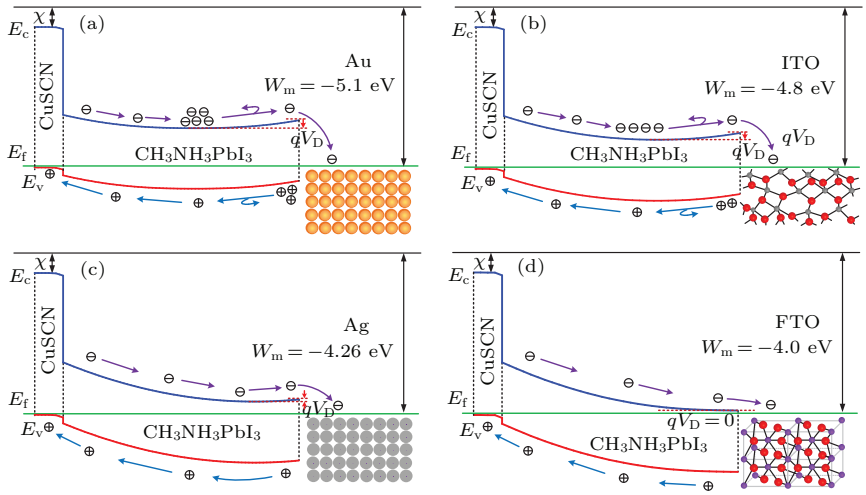


Fig. 6. Energy bands of CuSCN–$CH_3NH_3PbI_3$ with different electrode materials: (a) Au, (b) ITO, (c) Ag, (d) FTO.

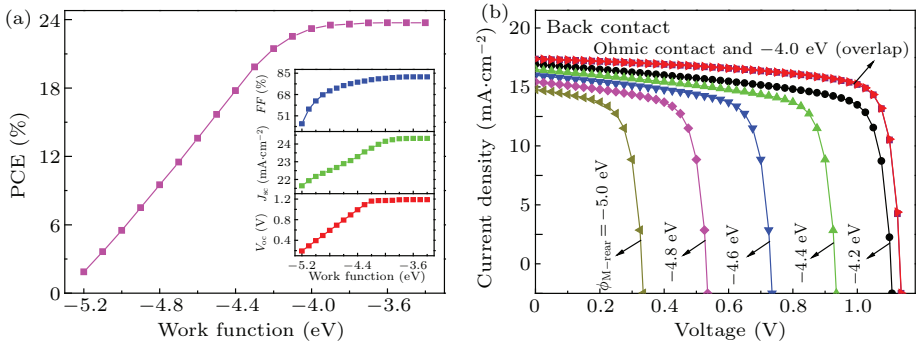


Fig. 7. (a) Device performance of CuSCN–$CH_3NH_3PbI_3$ *versus* work function of back electrode, and (b) *J*–*V* curves.

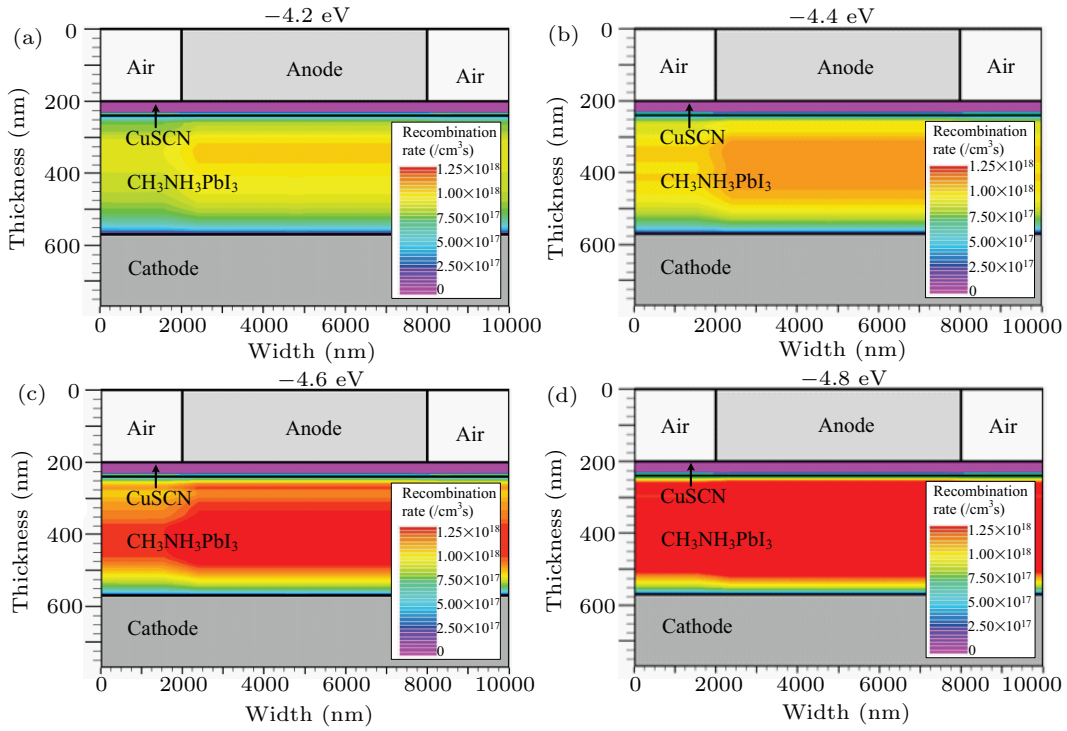


Fig. 8. Recombination rate distributions in CuSCN–$CH_3NH_3PbI_3$ PSC with different work functions of back electrode: (a) −4.2 eV, (b) −4.4 eV, (c) −4.6 eV, and (d) −4.8 eV.

Recombination loss occurs mainly in bulk of $CH_3NH_3PbI_3$ because of the energy band bending. Figure 8 shows that the recombination rate of carrier increases rapidly from 5.0×10^{17} cm^{-3}/s to 1.25×10^{18} cm^{-3}/s when the work junction of back electrode decreases from −4.2 eV to −4.8 eV. In view of this, the FTO with a work function of −4.0 eV is selected as an appropriate back electrode material.

3.4. Influence of band gap of $CH_3NH_3PbI_3$ on performance of CuSCN–$CH_3NH_3PbI_3$ PSC

The research shows that the band gap of perovskite (ABX_3) can be tuned in a range of 1.17 eV–4.09 eV by controlling the atomic ratio of Cs/FA/MA, Pb/Sn or I/Br/Cl.[30] Simultaneously, the gradient band gap perovskite can be fabricated by the ion exchange and spin coating method.[31,32] In this subsection, the effect of $CH_3NH_3PbI_3$ band gap on ETM-free PSC performance is investigated based on the former optimized HTM CuSCN, back electrode and $CH_3NH_3PbI_3$ thickness. The band gap distribution of $CH_3NH_3PbI_3$ has three structures according to the law of linear change, *i.e.* uniform structure, gradient decreasing structure, and gradient increasing structure (see Fig. 9).

Obviously, the photogenerated holes of gradient decreasing structure need to overcome an energy band barrier in the transport process, resulting in a large number of photogenerated holes remaining in the absorption layer and J_{sc} decreasing. Compared with uniform structure band gap and gradient decreasing structure band gap, the gradient increasing band gap can form a good valence band energy level that promotes hole transport and reduces carrier recombination loss.

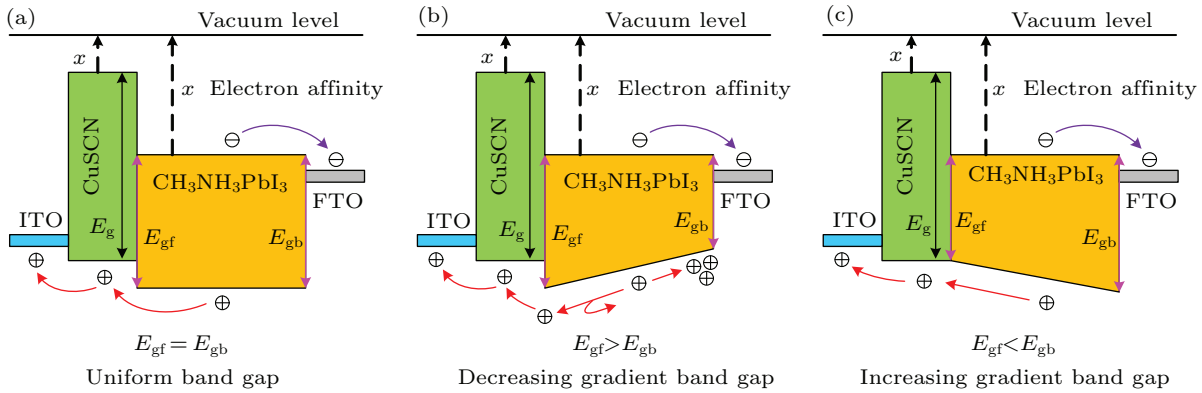


Fig. 9. Schematic diagram of CuSCN–$CH_3NH_3PbI_3$ PSC with different band gaps of $CH_3NH_3PbI_3$: (a) uniform structure, (b) gradient decreasing structure, and (c) gradient increasing structure.

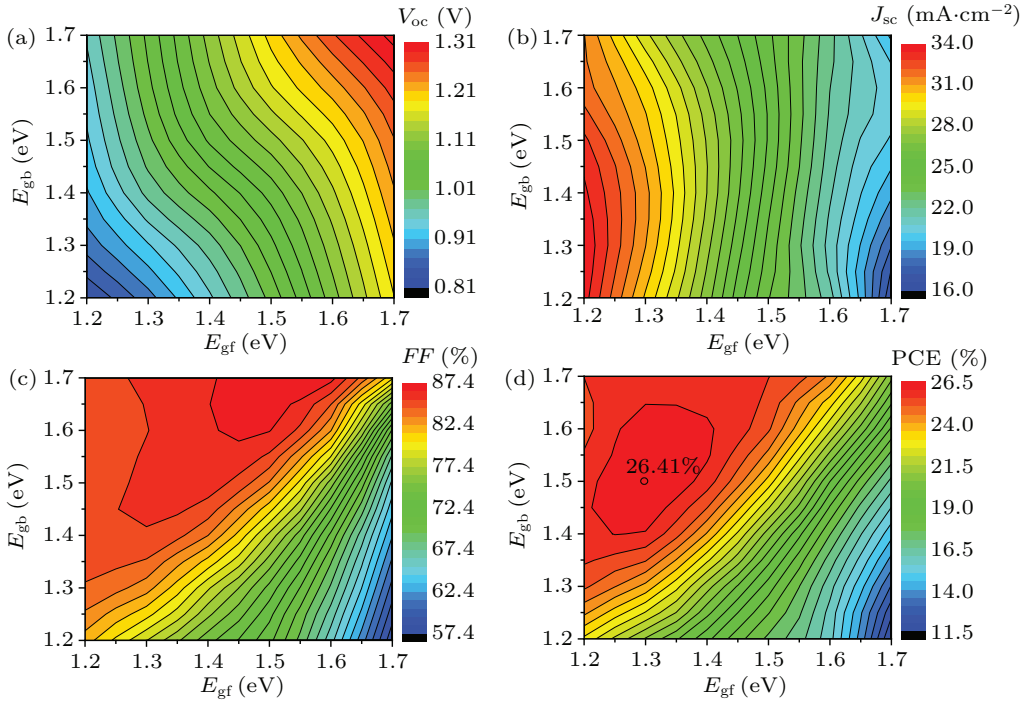


Fig. 10. Influences of $CH_3NH_3PbI_3$ band gap on performances of CuSCN–$CH_3NH_3PbI_3$ PSC, showing E_{gf}-dependent (a) V_{oc}, (b) J_{sc}, (c) FF, and (d) PCE.

The V_{oc}, J_{sc}, FF, and PCE of ITO–CuSCN–$CH_3NH_3PbI_3$–FTO PSCs varying with band gap of $CH_3NH_3PbI_3$ are depicted in Figs. 10(a)–10(b). The E_{gf} and E_{gb} represent the band gap of the front surface and back surface of $CH_3NH_3PbI_3$, respectively. The V_{oc} increases significantly with the increase of E_{gf} or E_{gb}. However, the effect of E_{gf} is stronger than that of E_{gb}. Because the PSC is irradiated from the front side, the number of the generated carriers is higher. Therefore, more carriers to separate at the front interface result in higher influence of E_{gf}. This also explains that the E_{gf} has a greater influence on the J_{sc}. The FF reaches a maximum value when E_{gf} is 1.4–1.5 eV and E_{gb} is 1.6–1.7 eV, which is because the difference in conduction band between the CuSCN interface and the $CH_3NH_3PbI_3$ interface is close to 0, resulting in the smallest parasitic resistance. Simultaneously, the gradient increasing structure forms when $E_{gb} > E_{gf}$, which accelerates hole drift and reduces the recombination rate. Finally, the PCE reaches a maximum value of 26.41% when $E_{gf} = 1.3$ eV and $E_{gb} = 1.5$ eV. Comparing with the uniform band gap of 1.55 eV, the optimization of the gradient band gap increases the PCE by 3.74% (see Table 4).

3.5. Influences of doping and defect of $CH_3NH_3PbI_3$ on property of CuSCN–$CH_3NH_3PbI_3$ PSC

Conductivity of material and built-in electric field of heterojunction are determined mainly by doping concentration of $CH_3NH_3PbI_3$ and HTM in ETM-free PSCs. In this subsection, the device performance of ITO–CuSCN–$CH_3NH_3PbI_3$–FTO PSC varying with donor concentration (N_d) of $CH_3NH_3PbI_3$ is discussed based on the former optimized $CH_3NH_3PbI_3$ thickness and band gap (see Fig. 11(a)). The V_{oc} increases linearly with N_d of $CH_3NH_3PbI_3$ increasing from 1.0×10^{15} cm^{-3} to 1.0×10^{18} cm^{-3} due to the fact that the fermi level of $CH_3NH_3PbI_3$ is closer to the conduction band minimum and the built-in electric field increases. The J_{sc} decreases significantly when N_d of $CH_3NH_3PbI_3$ exceeds 1.0×10^{16} cm^{-3}, which results from the width of space charge region decreasing, separation of electron-hole pair decreasing, and radiative recombination increasing. Optimal doping will increase conductivity and improve the FF. Finally, the PCE achieves a maximum value of 26.64% when N_d of $CH_3NH_3PbI_3$ is 5.0×10^{16} cm^{-3}.

The performance versus bulk defect density (N_t) of $CH_3NH_3PbI_3$ is presented. There are four types of bulk defects in material usually, *i.e.*, Gaussian acceptor defects, Gaussian donor defects, conductor-tail defects, and valence-tail defects. In this work, the influence of Gaussian acceptor defects in $CH_3NH_3PbI_3$ on PSC performance is studied (see Fig. 11(b)). The V_{oc}, J_{sc}, FF, and PCE of the PSC drop significantly when N_t exceeds 1.0×10^{15} cm^{-3}. Owing to the fact that the recombination rate increases with N_t increasing, and the concentration of majority carriers decreases, both built-in voltage of heterojunction and conductivity of material decrease. In order to achieve high efficiency, the bulk defect density in $CH_3NH_3PbI_3$ should be controlled to be less than 1.0×10^{15} cm^{-3}.

The influence of CuSCN thickness on the performance of CuSCN–$CH_3NH_3PbI_3$ PSC is shown in Fig. 11(c). The distance between photogenerated hole and electrode increases with the CuSCN thickness increasing, so the recombination

rate and the bulk resistance increase, which leads the J_{sc}, FF, V_{oc}, and PCE of the PSC to decrease linearly. As a result, the PCE of the PSC decreases by 0.3% when the thickness of CuSCN increases from 10 nm to 1000 nm. If the thickness of CuSCN decreases, the PCE of CuSCN–$CH_3NH_3PbI_3$ PSC will be improved.

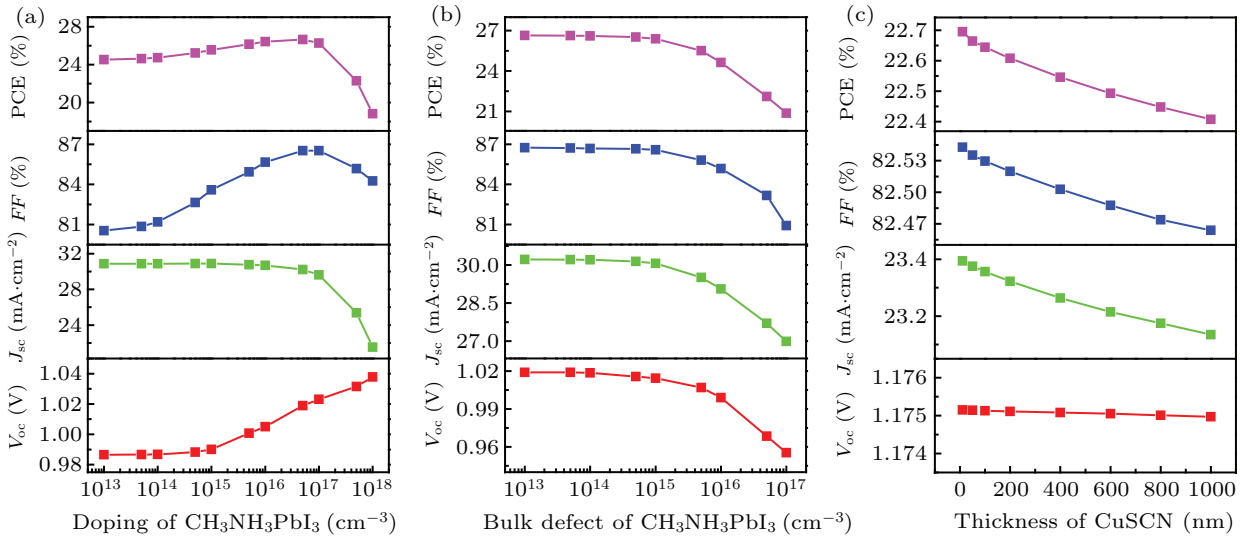


Fig. 11. Variations of CuSCN–$CH_3NH_3PbI_3$ cell performance with (a) doping of $CH_3NH_3PbI_3$, (b) bulk defect of $CH_3NH_3PbI_3$, and (c) thickness of CuSCN.

3.6. Influences of light and temperature on property of CuSCN–$CH_3NH_3PbI_3$ PSC

Figures 12(a) and 12(b) show that the electron current density and hole current density of the CuSCN–$CH_3NH_3PBI_3$ PSC significantly decrease under the solar irradiance from the vacuum environment (AM0) to the earth's surface (AM1.5), which leads to a smaller J–V characteristic and a 2.83% reduction in PCE.

As shown in Figs. 12(c)–12(d), the V_{oc} and PCE of PSC gradually decrease while the current density does not change significantly with the increase of temperature. Because the increase of temperature will cause the stress and strain to increase, which will lead the absorption layer the absorption layer to be distorted and disordered. Therefore, both the radiative recombination and the surface recombination of electron–hole pairs increase. Obviously, better photoelectric performance can be obtained in low temperature environment.

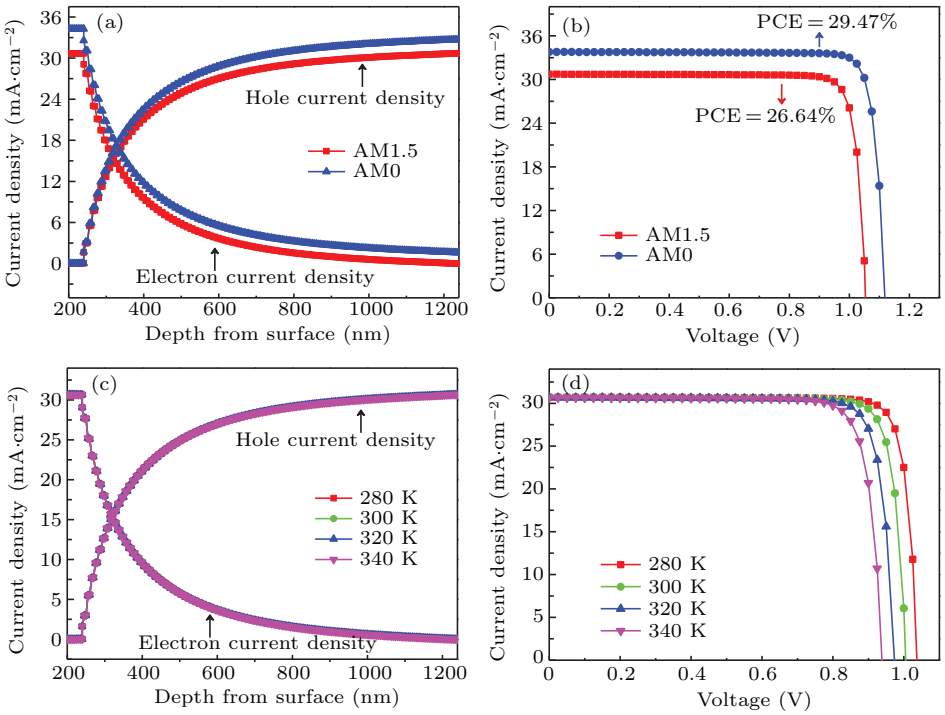


Fig. 12. Influences of light on performances of CuSCN–$CH_3NH_3PbI_3$ PSC: (a) current density and (b) J–V characteristics. Influences of temperature on performance CuSCN–$CH_3NH_3PbI_3$ PSC: (c) current density and (d) J–V characteristics.

Table 4. Performances of ITO–CuSCN–$CH_3NH_3PbI_3$–FTO during optimization.

ITO–CuSCN–$CH_3NH_3PbI_3$–FTO structure							
Optimization	Thickness (nm)	Band gap (eV)	Doping (cm^{-3})	V_{oc} (V)	J_{sc} ($mA{\cdot}cm^2$)	*FF* (%)	PCE (%)
Initial	330	uniform 1.55	1.0×10^{16}	1.14	20.64	79.07	18.56
$CH_3NH_3PbI_3$ thickness	1000	uniform 1.55	1.0×10^{16}	1.175	23.38	82.53	22.67
$CH_3NH_3PbI_3$band gap	1000	gradient 1.3–1.5	1.0×10^{16}	1.005	30.69	85.66	26.41
$CH_3NH_3PbI_3$ doping	1000	gradient 1.3–1.5	5.0×10^{16}	1.019	30.22	86.53	26.64

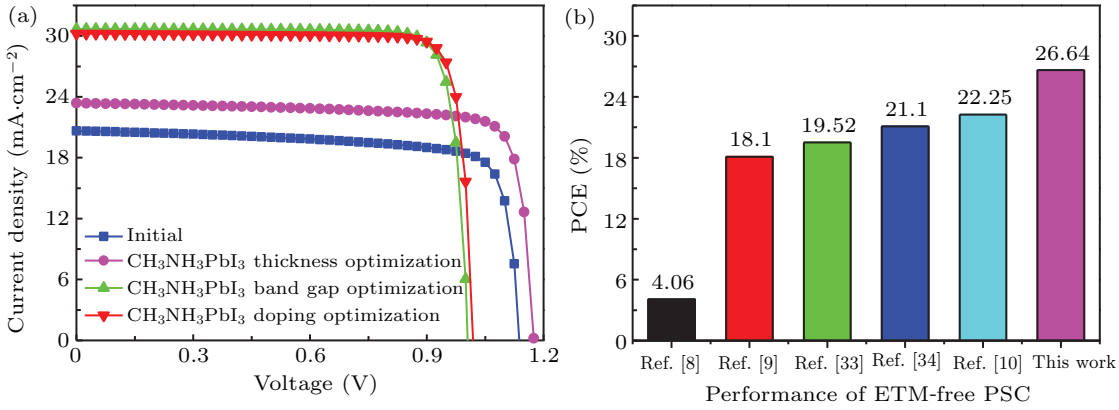


Fig. 13. (a) The *J*–*V* characteristics of ITO–CuSCN–$CH_3NH_3PbI_3$–FTO during optimization, (b) comparison among performances of ETM-free PSC cited from some reports.

In this paper, the structural advantages, material selection and some physical parameters of ETM-free PSC are studied in detail, and the PCE increases from 18.6% to 26.64% (see Table 4 and Fig. 13). However, there are still many aspects worth further studying. The first item is doping distribution types of the perovskite layer, *i.e.*, gradient type, exponential type or Gaussian type; the second item is the mobility of perovskite, which can be adjusted by changing the ratio of Sn/Pb atoms;[30] the third item is the designing of a double HTM to enhance the extraction velocity of photo-generated holes; the last item is the transparent conductive oxide FTO as the back electrode, which can further use diffuse reflected light to enhance cell efficiency.[35] These studies can provide a certain reference for the future researches.

4. Conclusions

Focused on CuSCN–$CH_3NH_3PbI_3$, a series of planar heterojunction PSCs with ETM-free structure and p–i–n structure are compared and numerically analyzed by the TCAD Atlas. Compared with PEDOT:PSS, Cu_2O, CuI, CuO, and NiO, the CuSCN is an excellent inorganic HTM for building ETM-free PSCs due to its high charge mobility, good energy band structure, and high EQE. Moreover, owing to the unique electric field structure, high conductivity and incident sunlight absorption, the performance of CuSCN–$CH_3NH_3PbI_3$ ETM-free PSC is better than those of p–i–n PSCs. Simultaneously, the gradient increasing band gap of $CH_3NH_3PbI_3$ can improve significantly the hole transport and increase J_{sc} and *FF*. Furthermore, the influences of the thickness, doping, and defect of $CH_3NH_3PbI_3$ on performance of CuSCN–$CH_3NH_3PbI_3$ PSC are analyzed in detail. The efficiency of ETM-free can be improved to 26.64% by CuSCN and gradient increasing $CH_3NH_3PbI_3$. Importantly, gradient band gap perovskite can be fabricated by ion exchange or spin coating technology, which is simple and low cost. This study provides a guide for designing and fabricating the ETM-free PSCs.

Acknowledgements

Project supported by the Fundamental Research Funds for the Central Universities of China (Grant No. JD2020JGPY0010) and the China Post-Doctoral Science Foundation (Grant No. 2020M671834).

References

[1] Green M A, Dunlop E D, Levi D H, Hohl-Ebinger J, Yoshita M and Ho-Baillie A W Y 2019 *Prog. Photovolt. Res. Appl.* **27** 565
[2] Heo J H, Han H J, Kim D, Ahn T K and Im S H 2015 *Energy Environ. Sci.* **8** 1602
[3] Meng L, You J, Guo T F and Yang Y 2016 *Acc. Chem. Res.* **49** 155
[4] Fu Q, Tang X L, Huang B, Hu T, Tan L C, Chen L and Chen Y W 2018 *Adv. Sci.* **5** 1700387
[5] Wang T, Wang P, Ding K and Liang Q 2019 *Optik* **179** 1019
[6] Said A A, Xie J and Zhang Q 2019 *Small* **15** 1900854
[7] Fan B, He Z, Xiong J, Zhao Q, Dai Z, Yang B, Xue X, Cai P, Zhan S, Tong S, Yang J and Zhang J 2019 *Sol. Energy* **189** 307
[8] Deng Y, Xiao Z and Huang J 2015 *Adv. Energy Mater.* **5** 1500721
[9] Chen T, Shi T, Li X, Zheng J, Fan W, Ni B, Wang Y, Dai J and Xiao Z 2018 *Solar RRL* **2** 1800167
[10] Sahu A and Dixit A 2018 *Curr. Appl. Phys* **18** 1583
[11] Niu G D, Li W Z, Li J W and Wang L D 2016 *Sci. China Mater.* **59** 728
[12] Elseman A M, Sajid S, Shalan A E, Mohamed S A and Rashad M M 2019 *Appl. Phys. A* **125** 464
[13] Chen J and Park N G 2018 *J. Phys. Chem. C* **122** 14039
[14] Minemoto T and Murata M 2014 *J. Appl. Phys.* **116** 054505

[15] Alnuaimi A, Almansouri I and Nayfeh A 2016 *J. Comput. Electron.* **15** 1110

[16] Karimi E and Ghorashi S M B 2017 *Optik* **130** 650

[17] Parhizkar M, Singh S, Nayak P K, Kumar N, Muthe K P, Gupta S K, Srinivasa R S, Talwar S S and Major S S 2005 *Colloids and Surfaces A: Physicochem. Eng. Aspects* **257–258** 277

[18] Shen Y, Guo M, Xia X and Shao G 2015 *Acta Mater.* **85** 122

[19] Hossain M I, Alharbi F H and Tabet N 2015 *Sol. Energy* **120** 370

[20] Zhao P, Liu Z, Lin Z, Chen D, Su J, Zhang C, Zhang J, Chang J and Hao Y 2018 *Sol. Energy* **169** 11

[21] Azri F, Meftah A, Sengouga N and Meftah A 2019 *Sol. Energy* **181** 372

[22] Chen C W, Hsiao S Y, Chen C Y, Kang H W, Huang Z Y and Lin H W 2015 *J. Mater. Chem. A* **3** 9152

[23] Steirer K X, Ndione P F, Widjonarko N E, Lloyd M T and Meyer J 2011 *Adv. Energy Mater.* **1** 813

[24] Abdulkarim Y I, Deng L, Muhammad F F and He L 2019 *Results Phys.* **13** 102338

[25] Claudia M, Francesco B, Cristy L A R, Mirco D I, Paolo S and Alberto M 2011 *Sol. Energy Mater. Sol. Cells* **95** 2848

[26] Ezealigo B N, Nwanya A C, Simo A, Bucher R, Osuji R U, Maaza M, Reddy M V and Ezema F I 2020 *Arab. J. Chem.* **13** 346

[27] Kariper I A 2016 *Mater. Res.* **19** 991

[28] Pandey R and Chaujar R 2016 *Superlattice Microst.* **100** 656

[29] Wang H, Yu Z, Lai J, Song X, Yang X, Hagfeldt A and Sun L 2018 *J. Mater. Chem. A* **6** 21435

[30] Du H J, Wang W C and Gu Y F 2017 *Chin. Phys. B* **26** 028803

[31] Fu F, Pisoni S, Weiss T P, Feurer T, Wackerlin A, Fuchs P, Nishiwaki S, Zortea L, Tiwari A N and Buecheler S 2018 *Adv. Sci.* **5** 1700675

[32] Ergen O, Gilbert S M, Pham T, Turner S J, Tan M T Z, Worsley M A and Zettl A 2016 *Nat. Mater.* **16** 522

[33] Han Q W, Ding J, Bai Y S, Liu J, Mitzi D B and Hu J S 2018 *Chem.* **4** 2405

[34] Wu W Q, Liao J F, Zhong J X, Xu Y F, Wang L Z and Huang J S 2020 *Angew. Chem. Int. Ed.* **59** 20980

[35] Lin J T, Lee C T, Chen W H, Haga S W, Hu Y Y and Ho K Y 2018 *IEEE J. Photovolt* **8** 441